2026 IEEE International Conference on Robotics and Automation (ICRA 2026)
June 1-5, 2026. Vienna, Austria

Wearable, Fabric-Embedded Acoustic Waveguides for Meter-Scale Contact Localization and Force Sensing

Wilfred Mason[1,2,†], Jad Ashkar[1], David Brenken[1,2], and Audrey Sedal[1,2,3]

***Abstract*— Large-area tactile sensing remains a key challenge for wearable and robotic applications, where solutions must balance resolution and complexity, manufacturability, and conformability to various geometries. While acoustic waveguides have been used for contact localization and force estimation at the centimeter scale, scaling this technology to limb-scale wearable devices is unexplored. In this work, we introduce a soft, wearable tactile sleeve based on wrapped and meter-length acoustic waveguides. By patterning waveguides on a sleeve, one-dimensional time-of-flight measurements are mapped to two-dimensional contact locations. This enables conformable coverage with sparse transducers, while preserving mechanical robustness by placing rigid electronics away from the contact surface. We contribute the design and fabrication of the waveguide-based tactile sensor, provide an in-depth characterization of sensor response and evaluate frameworks for contact localization and force estimation, and demonstrate system performance on a human arm. Results show that the time-of-flight-based localization approach generalizes across contact sizes and curved geometries. However, more work is required to achieve sensitive and reliable force estimates. This work establishes acoustic waveguides as a manufacturable and reconfigurable modality for wearable tactile skins.**

I. Introduction

Centimeter- to meter-scale tactile skins and textile wearables can enable safe and contact-aware human robot interaction [1], safety monitoring [2], closed-loop force and movement monitoring [3], [4], and learning of human-environment interactions [5]. These can be applied to rehabilitation and prosthetics, in the design of haptic communication interfaces for AR/VR and social interactions [6]–[8], and in home assistive robotics. Currently, there are few limb-scale tactile sensors that adequately capture diverse contact information (e.g., contact location, force, changes in contact over time) and that also meet the demands of wearable systems.

Dense tactile sensor arrays are candidates for limb-scale tactile sensing. Tactile sensor arrays can be realized by individually addressable taxels [3], [6], [9] or by matrix-addressed row-column grids. Matrix-addressed architectures include resistive textiles [5], [10], [11], capacitive skins [12], pneumatic taxel arrays [13], and waveguide networks [14]. Arrays enable straightforward reconstruction of force images, and garment-scale arrays can be mass-manufactured by knitting. However, scaling increases wiring complexity, readout latency, and the number of failure points and rigid electronics near the contact surface limit durability [15].

† Corresponding author. Email: wilfred.mason@mail.mcgill.ca
[1] Dept. of Mechanical Engineering, McGill University, Montreal, Canada.
[2] MILA–Quebec AI Institute.
[3] Centre for Intelligent Machines.

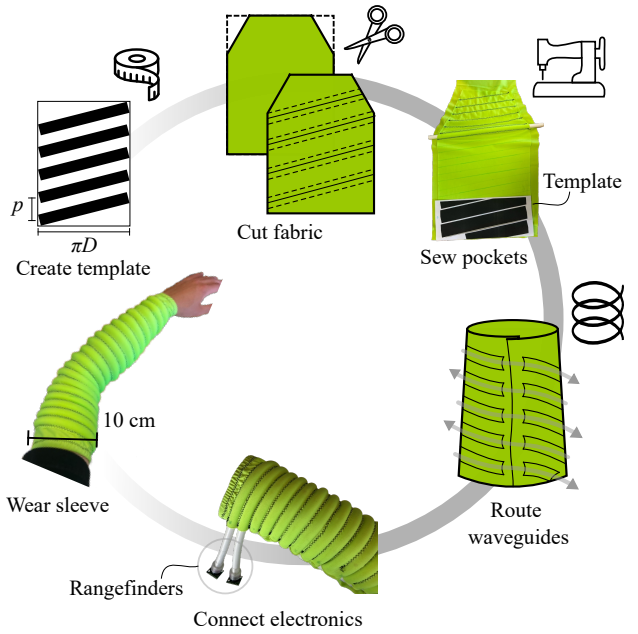

(a) Sensor manufacturing including sizing and cutting elastic fabric, sewing waveguide pockets, routing waveguides, and coupling an acoustic rangefinder to each waveguide. Tactile sensor sleeve design parameters indicated on template include waveguide pitch p and sleeve diameter D.

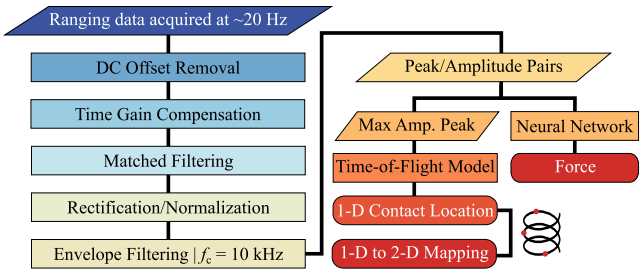

(b) Signal processing pipeline; rectangular blocks represent processing steps, parallelograms represent inputs and intermediate processed data, and rounded blocks represent outputs. f_c is the envelope cutoff frequency.

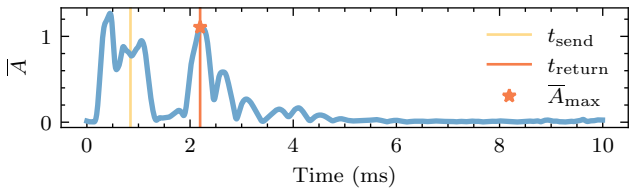

(c) Sample processed trace (time-gain compensated, match-filtered, rectified/normalized, low-pass-filtered). Send pulse time t_{send}, return pulse time t_{return}, and maximum normalized return pulse amplitude $\overline{A}_{\max}$ indicated.

Fig. 1. Wearable, limb-scale tactile sensor based on wrapped acoustic waveguides: design principle, manufacturing, and signal processing.

Distributed tactile sensing architectures infer contact location and magnitude with fewer measurement sites than arrays but suffer from drawbacks. Approaches using sparse transducers such as microphones [16] or fiber-Bragg gratings [17] require rigid or fragile hardware near the sensing surface, limiting mechanical robustness and wearability. Optical time-of-flight (ToF) methods constrain sensor geometry through precise source-receiver placement [18], while transmission-line ToF-based skins require custom liquid-metal conductors [19]. Other strategies rely on embodiment-specific calibration or sensor layout optimization [20]–[22].

An alternative strategy for sensorizing large surfaces is acoustic waveguides. Acoustic waveguides offer a wearable-friendly architecture for tactile sensing. They do not require a line-of-sight, they can be manufactured from a variety of flexible materials at different scales [23], [24], and they permit sparse transduction via ToF-based interrogation [25], addressing wiring, conformability, and mechanical robustness at body or robot scale. Furthermore, off-the-shelf (OTS) acoustic ranging and audio equipment are readily available and easy to integrate in waveguide-based sensors.

Existing work has focused on contact localization and force estimation in centimeter-length waveguides [24], [26], 2-D touch localization on centimeter-scale metamaterial lattices [27] and planar grippers [28], and the characterization of meter-length waveguides in planar [29] and circular configurations [23], [25]. In this work, we introduce a soft, wearable, conformable, and limb-scale tactile skin based on wrapped acoustic waveguides. Patterning waveguides on a sleeve converts 1-D ToF measurements into 2-D touch locations, offering large-area coverage with few transducers, mechanical robustness by keeping electronics off the contact surface, and geometric reconfigurability around joints. We contribute (i) the design and fabrication of an arm-scale tactile sensor based on acoustic waveguides, (ii) an in-depth characterization of sensor response and evaluation of frameworks for contact localization and force estimation, and (iii) a demonstration of touch localization on a human arm.

II. Methods

A. Sensor Design

The acoustic waveguides used in this work were OTS silicone rubber tubes (McMaster-Carr 5236K515) with inner diameter $D_i = 7.9\,\mathrm{mm}$, wall thickness $1.6\,\mathrm{mm}$, and Shore A hardness of 35. Waveguide parameters were chosen to balance sensing coverage, contact sensitivity, and resistance to buckling in the sleeve. Each waveguide was sensorized by an OTS acoustic rangefinder (MaxBotix MB1010 LV-MaxSonar-EZ1). The rangefinder emitted pulses with a frequency $f_{\text{send}} = 42\,\mathrm{kHz}$ and recorded reflections. Due to transducer ring-down, a ranging cycle was triggered every approximately $50\,\mathrm{ms}$ ($20\,\mathrm{Hz}$ refresh rate).

In this work, two waveguides were routed in a helical pattern in a bespoke fabric sleeve to create a wearable tactile sensor (Fig. 1(a)). To size the sleeve, we measured the wrist and forearm diameters of the wearer. We defined the helix pitch, waveguide pocket width, and the number of loops based on the desired sensing area. A template was used to cut two identical fabric layers from four-way stretch nylon spandex. The outlines of the waveguide pockets were transferred to the upper fabric layer using tailor's chalk. The two layers were sewn together along the pocket outlines using polyester thread and a zig-zag stitch pattern with a $3\,\mathrm{mm}$ pitch (Pfaff Varimatic 6085). Elastic straps were sewn into both ends of the sleeve before it was sewn closed with a zig-zag stitch. Two waveguides were routed through the pockets using a fused deposition modelling (FDM) 3-D printed polylactic acid (PLA) hollow cylinder (Bambu X1 Carbon). Each waveguide was mechanically coupled to a rangefinder using a 3-D printed adapter. $15\,\mathrm{cm}$ of waveguide length was left outside the sleeve. This region corresponded to a dead zone where contacts were not easily detected due to overlapping of reflected waves with the send pulse. The ends of each waveguide were terminated with polyurethane foam. Each waveguide was $250\,\mathrm{cm}$ long (9 loops), but attenuation limited the sensing range to below this maximum length.

B. Signal Processing

Raw ranging data was sampled at $f_s = 200\,\mathrm{kHz}$ and 12 bit resolution using the onboard ADC of a BeagleBone Black Industrial. We acquired 4000 samples from each ranging signal and recorded the temperature T. The ranging signal contained the send pulse and reflections from indentations along the waveguide. We applied the same signal processing pipeline to all ranging signals. First, we removed the DC offset from each signal using a low pass filter ($f_{\text{cutoff}} = 100\,\mathrm{Hz}$). We then applied time gain compensation (TGC) to the data to correct for signal attenuation. Next, we applied a matched filter to the amplified data using a Hann-windowed, ten-cycle sine wave template. We then rectified the ranging signal, normalized the data by the send pulse amplitude, and applied a low-pass filter ($f_{\text{cutoff}} = 10\,\mathrm{kHz}$). A summary of the signal processing chain and a sample processed trace is shown in Fig. 1(b) and Fig. 1(c) respectively. Candidate peaks are found using SciPy's `find_peaks` function [30] with an imposed minimum peak prominence `PP`.

1) Contact localization: The time t_{return} corresponding to the maximum amplitude peak in each ranging cycle was converted to a contact distance estimate $\ell_{\text{est.}}$ using a ToF model incorporating a temperature-dependent speed of sound [$c(T)$, SOS] and a calibrated send pulse reference time t_{send}:

$$\ell_{\text{est.}} = c(T)\frac{(t_{\text{return}} - t_{\text{send}})}{2}. \tag{1}$$

2) Force estimates: Force estimation was performed using a multilayer perceptron feed-forward neural network (MLP). The MLP's inputs were the peak amplitude and corresponding estimated distance in each ranging cycle and the outputs were the forces. The MLP architecture was a fully connected network, with an input layer of width 64, a hidden layer of width 64, and an output layer of width 1. We used Leaky ReLU as the activation function and He initialization for initial weighting [31]. Inputs and outputs were standardized on the training data mean and standard deviation. The

network was trained using 10-fold cross validation with 100 epochs, and a batch size of 32 using the Adam optimizer (learning rate 10^{-3}, weight decay 10^{-5}) and a loss function based on the mean squared error of force estimates. We did not observe clear overfitting based on validation loss curves. Force predictions were obtained by weighting each network by their normalized inverse validation loss.

C. 1-D to 2-D Contact Mapping

Contacts along the waveguide were mapped to locations on the sleeve. A motion capture setup (Vicon Vero) was used to estimate the parameters of the helices formed by the two waveguides (Fig. 7(a)). We placed two columns of reflective markers on the sleeve, the sleeve was then worn by the user, and we acquired marker coordinates while the arm was held straight. We fit a line with parameters (a_0, a_1) to each column of reflective markers to estimate the variable radius $r(z)$ of each helix as a function of the axial coordinate z (Fig. 7(b)). We estimated the twist rate of each helix based on the axial extent and number of loops $\rho = (2\pi \cdot n_{\text{loops}})/\Delta z_{\text{axial}}$. Each helix is then described by

$$\begin{aligned} r(z) &= a_0 + a_1\, z, \\ \psi(z) &= \rho\, z, \\ \mathbf{h}(z) &= \begin{bmatrix} r(z)\cos\big(\psi(z)\big) \\ r(z)\sin\big(\psi(z)\big) \\ z \end{bmatrix}. \end{aligned} \tag{2}$$

To map contact distances to spatial coordinates we built a lookup table by integrating the arc-length density $\ell'(z)$ along z. On an N-element grid $\{z_i\}_{i=0}^{N}$, we accumulated

$$\begin{aligned} \ell_{i+1} &= \ell_i + \tfrac{1}{2}\big[\ell'(z_i) + \ell'(z_{i+1})\big]\Delta z_i, \\ \ell'(z) &= \sqrt{1 + a_1^2 + \big(\rho\,(a_0 + a_1 z)\big)^2}, \end{aligned} \tag{3}$$

where $\ell_0 = 0$ and $\Delta z_i = z_{i+1} - z_i$.

D. Waveguide Simulations

We simulated the influence of indenter size on wave reflection characteristics such as maximum peak amplitude and ToF. We modelled waveguide deformation and acoustic wave propagation separately in ABAQUS (Fig. 2(a)). First, we deformed a straight, $40\,\text{cm}$-long waveguide with three cylindrical indenters $D_{\text{indenter}} \in \{10, 25, 35\}\,\text{mm}$ up to a depth of $D_{\text{wvg.}}$. We assumed a Neo-Hookean hyperelastic model with Poisson's ratio $\nu = 0.49$ and shear modulus $\mu = 10^{0.0235S - 0.64}/3$ (MPa) [32] where $S = 35$ was the Shore A hardness. We extracted the mesh of the deformed inner surface of the waveguide for different indentation depths. We then simulated time-domain wave propagation in the air-filled cavity of the waveguide for each deformed mesh. We imposed a uniform pressure input on one end of the waveguide (11-cycle Gaussian-modulated, sine wave) and an absorbing boundary condition on the other end to minimize the influence of end reflections on the ranging signal. We defined a measurement plane perpendicular to the waveguide axis and offset $2\,\text{cm}$ from the waveguide end and averaged nodal pressures on this plane to obtain ranging signals. Signals were then rectified, normalized, and low-pass filtered similar to the steps performed on experimental data.

E. Sensor Calibration

We performed a set of experiments to obtain the send pulse reference index and estimate the parameters of an attenuation model used for TGC. We calibrated the sensor by gathering data from complete blockages (Fig. 3(a)) along the waveguide at 37 locations $\ell_{\text{true}} \in \{20, 25, ..., 200\}\,\text{cm}$. The waveguide was completely blocked at each point using a 3-D printed cylinder. For each processed ranging cycle (DC-offset removed, rectified, enveloped), we extracted the peak with the highest normalized amplitude $\overline{A}_{\max}$ and computed its corresponding distance $\ell_{\text{est.}}$. We fit an attenuation model of the form in (4) with fitting parameters (c_1, c_2, c_3, c_4) between distances and peak amplitudes. In practice, using $\arctan$ for TGC introduced an increasing mean baseline trend that overwhelmed peaks at large distances. To prevent this, we used a hyperbolic tangent function with parameters from the $\arctan$ fit (i.e. $c_1 \tanh\left[c_2(\ell - c_3)\right] + c_4$). The $\tanh$ function has similar behaviour as the $\arctan$ function while resulting in smaller gain at large distances.

$$\overline{A}_{\max}(\ell) = c_1 \arctan\left[c_2(\ell - c_3)\right] + c_4 \tag{4}$$

Next we fit a line (slope and intercept) between true and estimated reflection distances. We initially set the send pulse reference time to be the time corresponding to the maximum amplitude in the send pulse. We then adjusted the send pulse time to minimize the intercept of the linear fit while maintaining the slope. We also acquired a set of ranging data in the waveguide without contacts. We performed the following processing steps on these data: DC-offset removal, TGC, matched filtering, rectification, and normalization. We then computed the standard deviation σ across ranging signals and obtained the peak prominence criteria for peak-finding ($\texttt{PP} = 2.8\sigma$). The scaling factor 2.8 was manually tuned to minimize false-positive peak detections.

F. Flat Configuration Study

We gathered two datasets for the waveguide in a flat configuration (Fig. 4(a)). For the first dataset, we statically indented the waveguide at evenly-spaced locations $\ell_{\text{true}} \in \{20, 21, ..., 210\}\,\text{cm}$ and indentation depths $\Delta x \in \{1, 1.5, ..., 8\}\,\text{mm}$ using a tensile testing machine (MTS C43, LPB.502). We used an FDM 3-D printed cylindrical indenter made of PLA with a diameter of $25\,\text{mm}$. For every distance and depth, we acquired approximately 50 ranging cycles over a $3\,\text{s}$ period starting $0.5\,\text{s}$ from the time when the indenter reached its set-point depth. We computed absolute errors between true and estimated distances, as well as median error, root mean square error (RMSE), and interquartile range (IQR) across the entire dataset. We used the maximum peak amplitudes, estimated contact distances, and ground-truth forces as training data for the MLP. For the second flat dataset, we gathered data from evenly-spaced distances $\ell_{\text{true}} \in \{20, ..., 160\}\,\text{cm}$ and 60 depths in the range $0.4\,\text{mm}$ to $8\,\text{mm}$. We used the second dataset to test the

force prediction MLP. We computed absolute error between true and estimated force as well as median error, RMSE, and IQR across the entire dataset.

G. Wrapped Configuration Study

1) Mannequin arm: We gathered depth, force, and ranging data from the tactile sleeve on a mannequin arm (Fig. 6(a)). We gathered data from seven locations and 15 indentation depths $\Delta x \in \{1, 1.5, ..., 8\}$ mm. We evaluated the absolute errors in force and location estimates and computed median error, RMSE, and IQR on the entire dataset.

2) Human arm: We gathered indentation data while a participant wore the tactile sensor (Fig. 7(a)). Using a push-pull probe, data was collected from seven regions on each waveguide at three force levels (2-4, 4-6, 6-8 N) for 2 s per location. Signals acquired at each location and force level were then averaged. We evaluated the absolute error in location, computed median error, RMSE, and IQR on the entire dataset, and reported the number of detected contacts at each force level. Due to the difficulty acquiring precise force data, we did not estimate force with this dataset.

III. Results

A. Waveguide Simulations

Fig. 2(b) shows amplitude variations for different indentation depths and indenter diameters. The amplitude trends are consistent across indenter sizes with the largest amplitudes occurring for the 10 mm indenter. Fig. 2(c) shows simulated reflected pulses for different indentation depths and diameters. The peak with the largest amplitude tracks the expected ToF for all indenter sizes with mean absolute errors and standard deviations of $(3.03 \pm 1.22\,\text{cm})$, $(2.95 \pm 1.92\,\text{cm})$, and $(2.51 \pm 1.64\,\text{cm})$ for the 10, 25, and 35 mm indenters, respectively. Reflections contain a variable number of peaks which are not consistent across indentation depths.

B. Sensor Calibration

Fig. 3 shows results from the calibration of the sensor. Fig. 3(b) shows true distance versus normalized amplitude along with the arctan and tanh fits. The arctan fit closely follows the experimental data (RMSE $= 0.0254$) except for distances close to the rangefinder. The tanh fit has a similar profile as the arctan fit with upper and lower horizontal asymptotes of $\overline{A} = 0.635$ and $\overline{A} = 0.104$ respectively. Fig. 3(c) shows true versus estimated distances. Estimates follow a linear trend except for distances close to the rangefinder. The slope of the line of best fit is 0.99 m/m (RMSE $= 36$ mm). For the remaining experiments, we probe the waveguide from 0.2 m to 2.1 m but search for peaks in the range 0.15 m to 2.15 m to account for localization error.

C. Flat Configuration Study

Fig. 4(c) shows true versus estimated contact distances. Most estimates lie close to the true distances. Outliers from shallow presses are predicted at 1.8 m. Fig. 4(d) shows mean absolute error (MAE) for each indentation depth and 38 true distance bins of width 5 cm. MAE is lowest for large

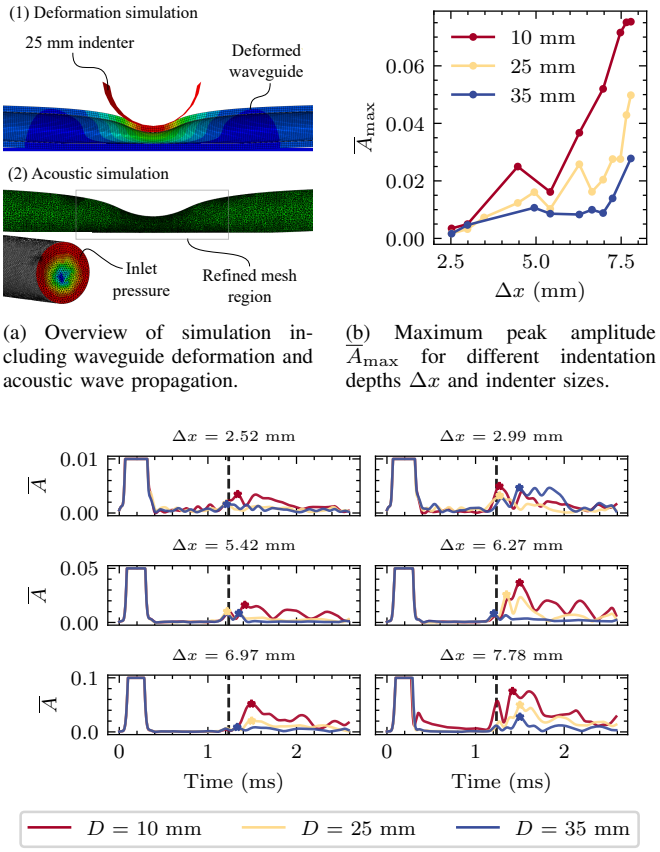

(a) Overview of simulation including waveguide deformation and acoustic wave propagation.

(b) Maximum peak amplitude $\overline{A}_{\max}$ for different indentation depths Δx and indenter sizes.

(c) Comparison of enveloped ranging signals ($f_{\text{cutoff}} = 10$ kHz) for different indenter diameters D and indentation depths Δx; $\overline{A}$ is the normalized reflected signal amplitude. Dashed lines indicate the expected arrival time (referenced to send-pulse center) and the stars indicate the normalized maximum amplitude peak in each signal. Send pulses are clipped to improve readability.

Fig. 2. Waveguide simulation results.

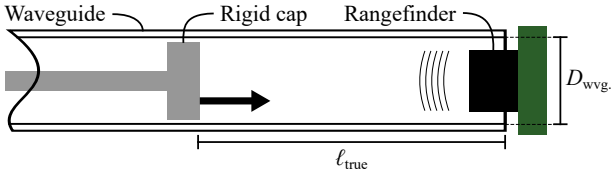

(a) Schematic of the experimental setup used for sensor calibration.

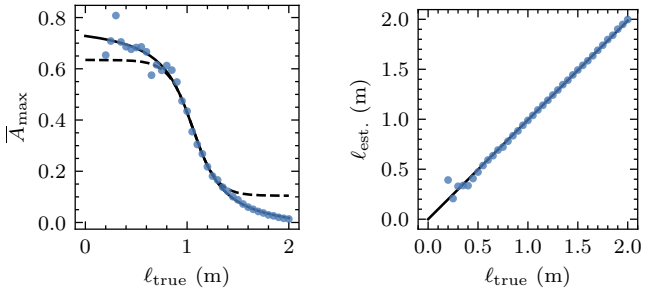

(b) Normalized amplitude of the highest return peak $\overline{A}_{\max}$ versus distance ℓ_{true}. arctan and tanh fits shown as solid and dashed lines.

(c) True ℓ_{true} versus estimated blockage distance $\ell_{\text{est.}}$. Linear fit shown as solid black line.

Fig. 3. Sensor calibration results.

indentation depths ($\Delta x > 6.5\,\text{mm}$) across all distances. MAE tends to increase at shallower depths. Contacts are not reliably detected for depths below approximately $2.5\,\text{mm}$. Only presses with depths surpassing $7\,\text{mm}$ are reliably detected at distances greater than approximately $1.95\,\text{m}$. Table I summarizes error metrics for contact localization.

Fig. 5(a) and 5(b) show variations in amplitude in a log scale across depths and distances. Amplitude increases monotonically with depth for distances less than approximately $0.60\,\text{m}$ and depths below $3.5\,\text{mm}$. For most distances, amplitude increases monotonically with depths greater than $6\,\text{mm}$. Amplitude variations are present for depths from $3.5\,\text{mm}$ to $6\,\text{mm}$, however, they are not monotonic. An MLP was trained to learn these complex amplitude variations.

Fig. 4(e) shows depth versus mean true force and estimated force and Fig. 4(f) shows mean absolute relative prediction error for each distance and depth. Force predictions from close contacts generally capture variations in force with depth (Fig. 4(e)). However, estimates across a large range of depths $3.5\,\text{mm} < \Delta x < 6\,\text{mm}$ tend to cluster about a mean value ($F \approx 4\,\text{N}$) and mean absolute relative error is high ($> 25\%$) across most of the domain (Fig. 4(f)). Median error, RMSE, and IQR are below $3\,\text{N}$ (Table II).

D. Wrapped Configuration Study

1) Mannequin arm: Fig. 6(c) shows true versus estimated contact distances on the mannequin arm. Contacts are resolved up to a distance of approximately $\ell = 2.1\,\text{m}$, however, only contacts corresponding to depths above $7\,\text{mm}$ are detected across the full range. Fig. 6(d) shows mean absolute localization errors with colours showing the average depth of samples within each bin. Observations are consistent with those from the flat configuration dataset; localization MAE is on average below $10\,\text{cm}$ for large indentation depths ($\Delta x > 6.5\,\text{mm}$) and increases for shallower indentations.

Fig. 6(e) shows depth versus mean true force and estimated force from the mannequin dataset and Fig. 6(f) shows mean absolute relative prediction error for each distance and depth. Observations are consistent with those from the flat configuration dataset; estimated force qualitatively tracks increases in force with depth but defaults to mean-value predictions across a large range of depths. Median error and IQR remain below $3\,\text{N}$, but RMSE is larger compared to the flat configuration dataset (Table II).

2) Human arm: Fig. 7(c) shows true versus estimated distances for the human arm dataset. Most estimated distances lie close to the true distance, with error tending to increase with decreasing force. Contacts are detected up to a distance of approximately $1.5\,\text{m}$. Three outliers (false-positive detections) occur at the largest distances. In general, fewer contacts from the lowest two force ranges are detected with increasing distance (Fig. 7(d)). Fig. 7(e) shows true contact locations and 12 estimated contact locations on one of the waveguides. Estimates lie close to the true locations, particularly for the highest force range presses. Localization error metrics on the human arm are consistent with the results from the flat configuration and mannequin datasets.

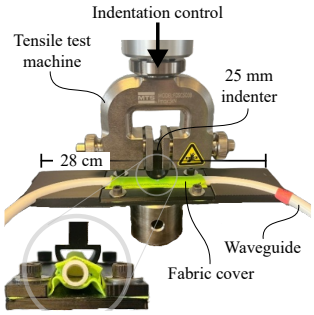

(a) Experimental setup.

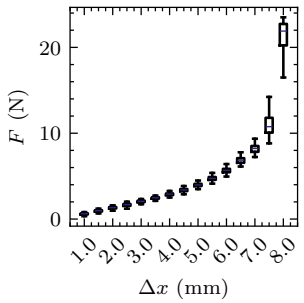

(b) Ground truth force F versus indentation depth Δx.

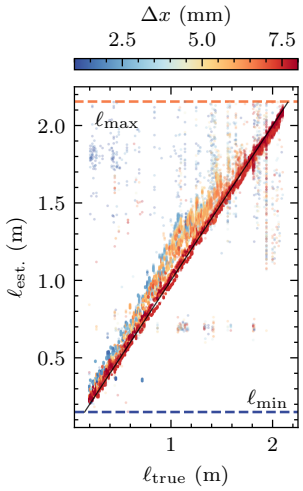

(c) True ℓ_{true} versus estimated distance $\ell_{\text{est.}}$. Colours indicate depth Δx. Distance search bounds $(\ell_{\min}, \ell_{\max})$ shown as dashed lines. 1:1 line shown in black.

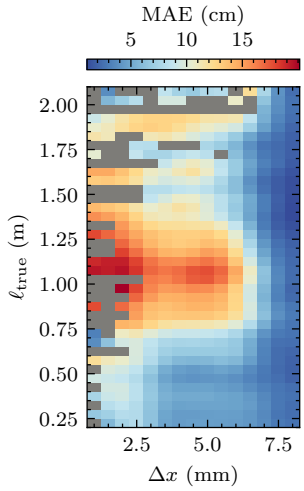

(d) Mean absolute error (MAE) of location estimates for 15 depths Δx and 38 true distance ℓ_{true} bins (Gaussian smoothed, $\sigma = 1$). Bins with no detected peaks or where MAE $> 25\,\text{cm}$ are gray.

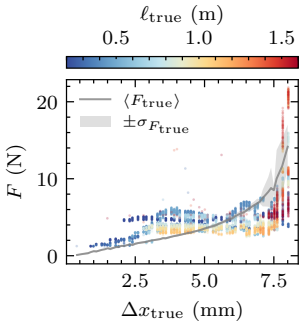

(e) Force predictions versus true depth Δx_{true}. Colours map to true distance. The gray line and shaded region show true force mean $\langle F_{\text{true}} \rangle$ and standard deviation $\sigma_{F_{\text{true}}}$.

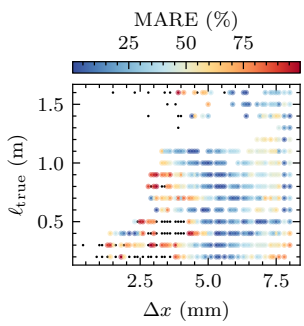

(f) Mean absolute relative error (MARE) of force estimates for each Δx level and ℓ_{true} level. Estimates where MARE $> 100\,\%$ are black.

Fig. 4. Flat configuration study results.

TABLE I

CONTACT LOCALIZATION ERROR SUMMARY.

Dataset	Median (cm)	RMSE (cm)	IQR (cm)
Flat Configuration	5.23	13.1	9.31
Mannequin Arm	8.48	14	12.9
Human Arm	3.8	14.5	11.7

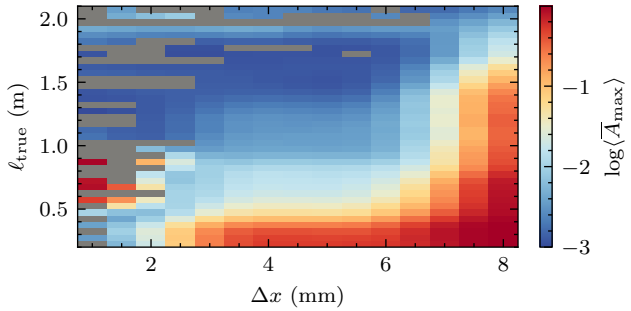

(a) First flat configuration dataset; mean log-scaled amplitudes from the highest normalized return peaks $\log\langle \overline{A}_{\max} \rangle$ for each indentation depth Δx and 38 true distance ℓ_{true} bins (Gaussian smoothed, $\sigma = 1$). Bins with no detected peaks or where MAE > 25 cm are gray.

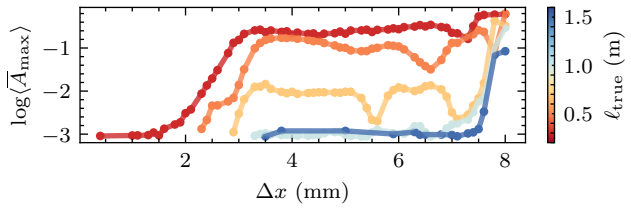

(b) Second flat configuration dataset; mean log-scaled amplitudes from the highest normalized return peaks $\log\langle \overline{A}_{\max} \rangle$ for each indentation depth Δx and five true distances ℓ_{true}.

Fig. 5. Amplitude trends from the flat configuration study.

TABLE II
FORCE ESTIMATION ERROR SUMMARY FOR THE FLAT CONFIGURATION (FLAT CON.) AND MANNEQUIN ARM (MANN.) DATASETS
(MEDARE: MEDIAN ABSOLUTE RELATIVE ERROR).

Dataset	Median (N)	RMSE (N)	IQR (N)	MedARE (%)
Flat Con.	1.49	2.95	2.09	41.8
Mann.	2.19	5.61	2.79	59.2

IV. DISCUSSION

The simulation results suggest that ToF arrivals are not significantly influenced by indenter size. Future work should experimentally validate these observations and the generalization of the ToF localization framework to other contact geometries. The results from all experiments indicate that the ToF-based localization model is most accurate at large indentation depths. At shallower indentations, the ToF model appears to be governed by a depth-dependent SOS. In contrast, the simulations show limited variance of distance estimates with indentation depth. This suggests that depth-dependent SOS may also be influenced by the coupling between cavity waves and the waveguide's compliant walls, rather than variations in tube geometry alone. This coupling is currently not modelled in simulations.

The results from the mannequin arm experiments indicate that ToF-based localization generalizes to helical waveguide configurations. Lower median error in the human arm dataset is likely due to the higher proportion of large force contacts compared to the other datasets. Transferring from the mannequin arm to the human arm results in a decrease in the sensing range. The decreased range of the sensor in the wearable embodiment could be due to higher attenuation

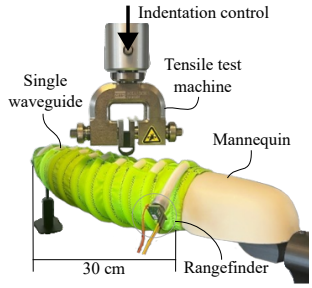

(a) Experimental setup.

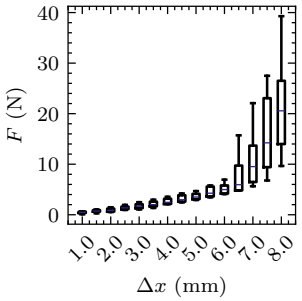

(b) Ground truth force F versus indentation depth Δx.

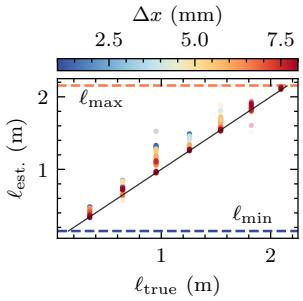

(c) True ℓ_{true} versus estimated distance $\ell_{\text{est.}}$. Colours indicate depth Δx. Distance search bounds $(\ell_{\min}, \ell_{\max})$ shown as dashed lines. 1:1 line shown in black.

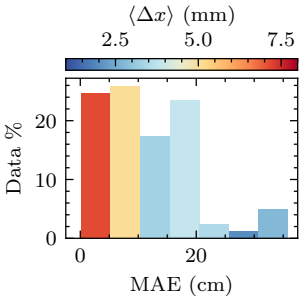

(d) Distribution of mean absolute errors (MAE) computed for each depth/distance pair in the dataset. Bars in the histogram are coloured according to average depth $\langle \Delta x \rangle$.

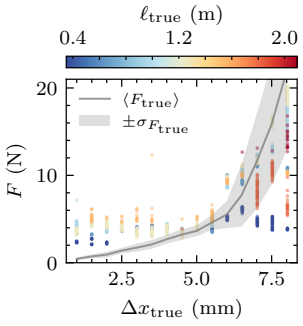

(e) Force predictions versus true depth Δx_{true}. Colours map to true distance. The gray line and shaded region show true force mean $\langle F_{\text{true}} \rangle$ and standard deviation $\sigma_{F_{\text{true}}}$.

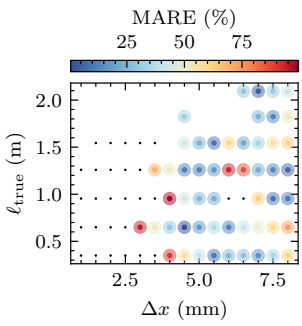

(f) Mean absolute relative error (MARE) of force estimates for each Δx level and ℓ_{true} level. Estimates where MARE $> 100\,\%$ are black.

Fig. 6. Wrapped configuration (mannequin arm) study results.

in the waveguide caused by narrowing of the waveguide on the stretched sleeve. A looser fit could improve signal transmission. The sensing range can also be increased by adding another set of rangefinders to the waveguide ends and by optimizing waveguide number and patterning. Overall, the performance of the sensor is sufficient for coarse contact localization. Contacts can be estimated within a loop on the sleeve and migrating contacts (e.g. from swipe-like presses) can possibly be tracked along the central axis of the helix. Given system sensitivity to indentation depth, increasing waveguide compliance should improve localization accuracy.

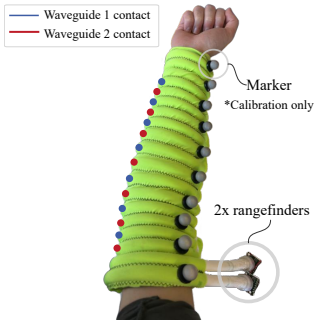

(a) Sensor worn by participant. Markers removed before testing.

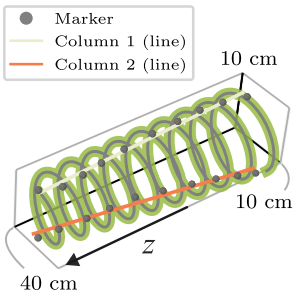

(b) Helix fitting process. Nine waveguide loops displayed.

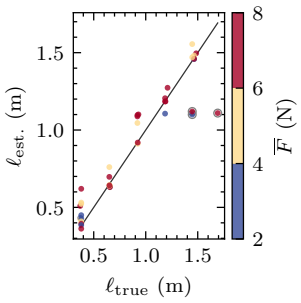

(c) True ℓ_{true} versus estimated $\ell_{\text{est.}}$ distances for three force levels on both waveguides. Estimates where the absolute error exceeded 25 cm are circled in gray.

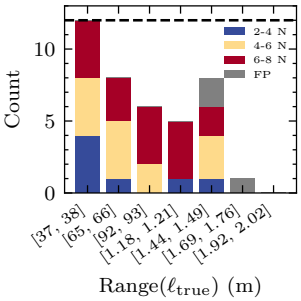

(d) Detected contacts (count) for each force and distance range Range(ℓ_{true}). False-positive (FP) estimates where the absolute error exceeded 25 cm are coloured in gray.

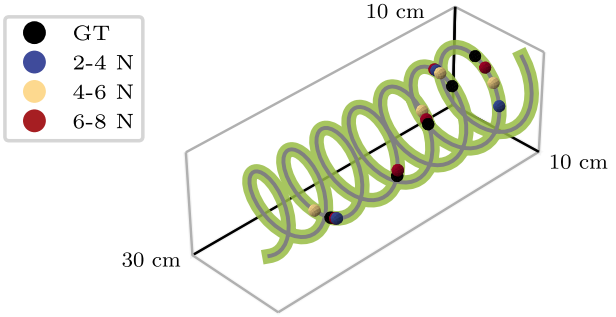

(e) Overlay of ground truth (GT) and 12 estimated contact locations for three force levels on one waveguide. Seven waveguide loops displayed.

Fig. 7. Wrapped configuration (human arm) study results.

The results indicate that forces can only be estimated reliably across a limited range and predictions tend to cluster around a mean value. Poor force estimation accuracy is likely due to the lack of monotonic variations of amplitude with force for certain depths and distances. Force estimates can potentially be improved by operating below the first cutoff frequency for a cylindrical waveguide [$f_{\text{send}} < 1.84c/(\pi D_i)$, where c is the SOS in air [33]]. The first cutoff frequency corresponds to the threshold frequency below which higher-order acoustic modes cannot propagate. Below the cut-off, only the plane-wave mode propagates, and the force-amplitude trends should follow a monotonic relationship that depends on the area change of the indented waveguide [29]. However, the influence of waveguide compliance in the sub-cutoff regime remains to be characterized. Future work should optimize waveguide material and geometry to ensure a consistent area change across the range of press depths.

In the current embodiment, fewer shallow contacts are detected at large distances due to their low amplitude. This creates a sampling bias where contacts at large distances are represented by higher forces. Consequently, the model tends to default to mean-force predictions across a range of distances rather than disentangling force-dependent amplitude variations from distance-dependent attenuation. Strategies for reducing waveguide attenuation should improve detection of shallower presses and enable force estimation across the full range of distances. Finally, contact with the test platforms introduced significant force variance at large depths (Fig. 6(b)). Since force is intrinsically coupled to substrate compliance (e.g., human arm vs. rigid robot), future work should estimate indentation depth as a substrate-independent quantity.

V. Conclusion

This work introduces a new sensing modality for creating limb-scale tactile skins for wearable applications. The sensor is conformable, has a simple and repeatable manufacturing process, and eliminates the wiring complexity of sensor arrays. The ability to localize contacts on multiple patterned waveguides can enable gesture detection and estimates of contact size (see supplementary video). In future work, the hollow waveguides can be pneumatically pressurized, creating haptic garments with combined sensing and actuation [34]. Proprioceptive capability can be added to the tactile sleeve by embedding OTS flex sensors [35]. The main limitation of this work is the limited accuracy of the force estimation pipeline. However, avenues for improving force accuracy by operating below the waveguide cutoff frequency [29] and optimizing the waveguide parameters to maximize changes in reflected signal characteristics across the full range of press depths are promising. The simulation tool presented here can be used to model both waveguide deformation and global trends in acoustic response. More realistic estimates can likely be obtained by considering the coupling between the structural and acoustic domains. Altogether, the results establish acoustic waveguides as a general, manufacturable route to achieve large-area tactile sensing combining conformable layouts and sparse I/O. While force estimation remains a challenge, the distributed contact localization capabilities of the sensor, driven by a generalizable ToF-based algorithm, open the door for more advanced functionality in both wearable and robotic systems.

Acknowledgment

The authors thank the members of the MACRObotics Research Group as well as Madison Odabassian, Kenz Zaghib, and Olivier St-Martin Cormier for their continual advice and support. This work was supported in part by Fonds de Recherche du Québec Nature et Technologies and in part by Meta Reality Labs.

REFERENCES

[1] A. Goncalves, N. Kuppuswamy, A. Beaulieu, A. Uttamchandani, K. M. Tsui, and A. Alspach, "Punyo-1: Soft tactile-sensing upper-body robot for large object manipulation and physical human interaction," in *2022 IEEE 5th International Conference on Soft Robotics (RoboSoft)*. IEEE, 2022, pp. 844–851.

[2] K. C. Welch, C. Harnett, and Y.-C. Lee, "A review on measuring affect with practical sensors to monitor driver behavior," *Safety*, vol. 5, no. 4, p. 72, 2019.

[3] B. Xu, L. Zhong, G. Zhang, X. Liang, D. Virtue, R. Madan, and T. Bhattacharjee, "Cushsense: Soft, stretchable, and comfortable tactile-sensing skin for physical human-robot interaction," in *2024 IEEE International Conference on Robotics and Automation (ICRA)*. IEEE, 2024, pp. 5694–5701.

[4] A. P. Gerratt, H. O. Michaud, and S. P. Lacour, "Elastomeric electronic skin for prosthetic tactile sensation," *Advanced Functional Materials*, vol. 25, no. 15, pp. 2287–2295, 2015.

[5] Y. Luo, Y. Li, P. Sharma, W. Shou, K. Wu, M. Foshey, B. Li, T. Palacios, A. Torralba, and W. Matusik, "Learning human–environment interactions using conformal tactile textiles," *Nature Electronics*, vol. 4, no. 3, pp. 193–201, 2021.

[6] B. Shao, M.-H. Lu, T.-C. Wu, W.-C. Peng, T.-Y. Ko, Y.-C. Hsiao, J.-Y. Chen, B. Sun, R. Liu, and Y.-C. Lai, "Large-area, untethered, metamorphic, and omnidirectionally stretchable multiplexing self-powered triboelectric skins," *Nature Communications*, vol. 15, no. 1, p. 1238, 2024.

[7] W. Yang, S. Lin, W. Gong, R. Lin, C. Jiang, X. Yang, Y. Hu, J. Wang, X. Xiao, K. Li *et al.*, "Single body-coupled fiber enables chipless textile electronics," *Science*, vol. 384, no. 6691, pp. 74–81, 2024.

[8] X. L. Cang and A. Israr, "Communicating socio-emotional sentiment through haptic messages," in *IEEE Haptics Symposium HAPTICS*, 2020.

[9] M. L. Preti, P. Trunin, D. Cafiso, and L. Beccai, "The hexsows: a modular soft and robust skin concept for multimodal tactile sensing," in *2025 IEEE 8th International Conference on Soft Robotics (RoboSoft)*. IEEE, 2025, pp. 1–8.

[10] B. Y. Su, Z. Wei, J. McCann, W. Yuan, and C. Liu, "Customizing textile and tactile skins for interactive industrial robots," *ASME Letters in Dynamic Systems and Control*, vol. 3, no. 3, p. 031007, 2023.

[11] M. Inaba, Y. Hoshino, K. Nagasaka, T. Ninomiya, S. Kagami, and H. Inoue, "A full-body tactile sensor suit using electrically conductive fabric and strings," in *Proceedings of IEEE/RSJ International Conference on Intelligent Robots and Systems. IROS'96*, vol. 2. IEEE, 1996, pp. 450–457.

[12] M. Teyssier, B. Parilusyan, A. Roudaut, and J. Steimle, "Human-like artificial skin sensor for physical human-robot interaction," in *2021 IEEE International Conference on Robotics and Automation (ICRA)*. IEEE, 2021, pp. 3626–3633.

[13] X. Zha, S. Jadhav, I. Adibnazari, Y. Zhai, and M. T. Tolley, "Scalable arrays of pneumatic sensors for multitouch soft skins," in *2024 IEEE 7th international conference on soft robotics (RoboSoft)*. IEEE, 2024, pp. 1088–1094.

[14] Y. Wang, C. Sun, and D. Ahmed, "A smart acoustic textile for health monitoring," *Nature Electronics*, vol. 8, no. 6, pp. 485–495, 2025.

[15] R. Dahiya, N. Yogeswaran, F. Liu, L. Manjakkal, E. Burdet, V. Hayward, and H. Jörntell, "Large-area soft e-skin: The challenges beyond sensor designs," *Proceedings of the IEEE*, vol. 107, no. 10, pp. 2016–2033, 2019.

[16] K. Park, H. Yuk, M. Yang, J. Cho, H. Lee, and J. Kim, "A biomimetic elastomeric robot skin using electrical impedance and acoustic tomography for tactile sensing," *Science Robotics*, vol. 7, no. 67, p. eabm7187, 2022.

[17] X. Dong, C.-K. Lam, W. Chen, B. Yang, and Y.-H. Liu, "A robotic skin using low-density fbgs for human-robot interaction," in *2024 IEEE International Conference on Robotics and Biomimetics (ROBIO)*. IEEE, 2024, pp. 129–134.

[18] E. Bacher, S. Cartiel, J. García-Pueyo, J. Stopar, A. Zore, R. Kamnik, I. Aulika, A. Ogurcovs, J. Grūbe, A. Bundulis *et al.*, "Optoskin: Novel lidar touch sensors for detection of touch and pressure within wave guides," *IEEE Sensors Journal*, vol. 24, no. 20, pp. 33 268–33 280, 2024.

[19] A. Leber, C. Dong, R. Chandran, T. Das Gupta, N. Bartolomei, and F. Sorin, "Soft and stretchable liquid metal transmission lines as distributed probes of multimodal deformations," *Nature Electronics*, vol. 3, no. 6, pp. 316–326, 2020.

[20] J. A. Barreiros, A. Xu, S. Pugach, N. Iyengar, G. Troxell, A. Cornwell, S. Hong, B. Selman, and R. F. Shepherd, "Haptic perception using optoelectronic robotic flesh for embodied artificially intelligent agents," *Science Robotics*, vol. 7, no. 67, p. eabi6745, 2022.

[21] S. S. Bae, T. Fujiwara, A. Ynnerman, E. Y.-L. Do, M. L. Rivera, and D. A. Szafir, "A computational design pipeline to fabricate sensing network physicalizations," *IEEE Transactions on Visualization and Computer Graphics*, vol. 30, no. 1, pp. 913–923, 2023.

[22] H. A. Sonar, M. C. Yuen, R. Kramer-Bottiglio, and J. Paik, "An any-resolution pressure localization scheme using a soft capacitive sensor skin," in *2018 IEEE International Conference on Soft Robotics (RoboSoft)*. IEEE, 2018, pp. 170–175.

[23] W. Mason, D. Brenken, O. S.-M. Cormier, and A. Sedal, "They hear me rolling: Design and characterization of a distributed, rolling acoustic-tactile sensor," *IEEE Sensors Letters*, 2025.

[24] Y. Lin and P. B. Shull, "Novel, soft, water-filled acoustic waveguides for simultaneous tactile force and location sensing," *IEEE Transactions on Industrial Electronics*, vol. 71, no. 7, pp. 8141–8155, 2023.

[25] C. E. Tejada, J. McIntosh, K. A. Bergen, S. Boring, D. Ashbrook, and A. Marzo, "Echotube: Robust touch sensing along flexible tubes using waveguided ultrasound," in *Proceedings of the 2019 ACM international conference on interactive surfaces and spaces*, 2019, pp. 147–155.

[26] Z. Li, Y. Lin, P. B. Shull, and H. Ren, "Disentangling contact location for stretchable tactile sensors from soft waveguide ultrasonic scatter signals," *Advanced Intelligent Systems*, vol. 7, no. 5, p. 2400561, 2025.

[27] J. Yang, Y. Sun, J. Zhang, C. Feng, X. Chen, and L. Bai, "Interpenetrating phase composite graded lattice structure integrated with load-bearing and sensing capabilities," *Composites Part A: Applied Science and Manufacturing*, vol. 164, p. 107294, 2023.

[28] S. Parsons, A. Ghalamzan *et al.*, "Single and bi-layered 2-d acoustic soft tactile skin," in *2024 IEEE 7th international conference on soft robotics (RoboSoft)*. IEEE, 2024, pp. 133–138.

[29] K. Nakamura, S. Odajima, and M. Tabaru, "Distributed force sensor based on acoustic characteristics of elastic tube," *Acoustical Science and Technology*, vol. 38, no. 2, pp. 80–86, 2017.

[30] P. Virtanen, R. Gommers, T. E. Oliphant, M. Haberland, T. Reddy, D. Cournapeau, E. Burovski, P. Peterson, W. Weckesser, J. Bright, S. J. van der Walt, M. Brett, J. Wilson, K. J. Millman, N. Mayorov, A. R. J. Nelson, E. Jones, R. Kern, E. Larson, C. J. Carey, İ. Polat, Y. Feng, E. W. Moore, J. VanderPlas, D. Laxalde, J. Perktold, R. Cimrman, I. Henriksen, E. A. Quintero, C. R. Harris, A. M. Archibald, A. H. Ribeiro, F. Pedregosa, P. van Mulbregt, and SciPy 1.0 Contributors, "SciPy 1.0: Fundamental Algorithms for Scientific Computing in Python," *Nature Methods*, vol. 17, pp. 261–272, 2020.

[31] K. He, X. Zhang, S. Ren, and J. Sun, "Delving deep into rectifiers: Surpassing human-level performance on imagenet classification," in *Proceedings of the IEEE international conference on computer vision*, 2015, pp. 1026–1034.

[32] H. Qi, K. Joyce, and M. Boyce, "Durometer hardness and the stress-strain behavior of elastomeric materials," *Rubber chemistry and technology*, vol. 76, no. 2, pp. 419–435, 2003.

[33] N. H. Fletcher and T. D. Rossing, *The physics of musical instruments*. Springer Science & Business Media, 2012.

[34] M. Zhu, T. N. Do, E. Hawkes, and Y. Visell, "Fluidic fabric muscle sheets for wearable and soft robotics," *Soft robotics*, vol. 7, no. 2, pp. 179–197, 2020.

[35] A. Sepehri, M. T. Tolley, and T. K. Morimoto, "Retrofitting soft assistive robots with sew-free sensing garments for joint motion tracking and kinematic feedback," in *2025 International Conference On Rehabilitation Robotics (ICORR)*. IEEE, 2025, pp. 1–7.